

Propagation and Attenuation Characteristics of Ground Vibrations: Beijing High Energy Photon Source (HEPS)

Experiments and Intelligent Law Discovery

Pei-Yao Chen^{a,1}, Chen Wang^{a,1}, Fang Yan^{b,c,*}, Chao-Yang Zhang^{b,d},
Xiang-Yu Tan^{b,c}, Guo-Ping Lin^b, Jian-Sheng Fan^a

^a Department of Civil Engineering, Tsinghua University, Beijing 100084, China

^b Institute of High Energy Physics, Chinese Academy of Sciences, Beijing, 100049, China

^c University of the Chinese Academy of Sciences, Beijing, 100049, China

^d College of Water Resources and Civil Engineering, China Agricultural University, Beijing, 100083, China

* Corresponding Author

E-mail addresses: pyaoch@163.com (P. Chen), qtwjy309@163.com (C. Wang), yanfang@ihep.ac.cn (F. Yan), zhangchy@ihep.ac.cn (C. Zhang), xytan@ihep.ac.cn (X. Tan), lingp@ihep.ac.cn (G. Lin), fanjsh@tsinghua.edu.cn (J. Fan)

¹ The two authors contribute equally to this work

Abstract

The propagation and attenuation characteristics of ground vibrations are of significant importance for assessing the interference of environmental factors, such as vehicles, on precision instruments. To investigate the impact of ground vibrations on the Beijing High Energy Photon Source (HEPS). This study conducted swept-frequency excitation tests at the HEPS site using an electrodynamic vibrator operating within the 1–100 Hz frequency range. Based on the experimental data, a hybrid iterative fitting method combining machine learning and formulaic intelligent generation is proposed, utilizing the Bornitz formula as the foundation. Through a data-driven approach, the propagation and attenuation laws of ground vibrations are formulated. The computational error of the formula is estimated using probabilistic analysis, and the physical rationality of the formula is elucidated. Finally, by comparing the proposed method with empirical formulas from previous studies and black-box machine learning models, it is demonstrated that the method introduced in this research offers substantial advantages in terms of accuracy and interpretability. This method holds universal value for the discovery of the propagation and attenuation laws of ground vibrations.

Keywords: ground vibrations; propagation and attenuation; filed test; machine learning; formula discovery

1. Introduction

The propagation and attenuation of vibrations have important applications in fields such as transportation [1,2], pipelines [3,4], environmental engineering [5,6], and damage detection [7–10]. With the advancement of technology, the infrastructure supporting high-precision technologies demands stringent control over vibrations. Ground vibrations, a common form of vibration resulting from human activities such as vehicles and railways [11–13], have a significant impact on the performance of sensitive equipment. Therefore, understanding the propagation and attenuation mechanisms of these vibrations is essential for evaluating their effects on precision instruments. However, the complexity of soil properties and environmental factors such as reflection and interference, caused by site conditions, make the propagation and attenuation behaviors of ground vibrations highly intricate. Thus, it is necessary to conduct field experiments and derive the propagation and attenuation patterns of ground vibrations from the experimental data.

The study of ground vibration propagation and attenuation is generally approached through a combination of theoretical models and field experiments. Yang et al. [14] proposed an analytical solution for the ground vibration of a half-space induced by sub- and super-critical harmonic moving loads, employing a contour integral combined with the residue theorem. Wu et al. [15] investigated the propagation and attenuation of elastic waves in multi-row infinitely periodic pile barriers, validating their findings through several numerical cases. Wang et al. [16] characterized the vibration effects and developed a real-time statistical method for attenuation of vibration effects during continuous ground-penetrating radar surveys. The processing time of this method is within seconds, enabling real-time and

automatic attenuation of vibration effects. Zarei et al. [17] comprehensively evaluates the vibrations induced by heavy vehicles on asphalt pavements, developing a 2.5D finite element model to analyze the impact of vehicle speed and bump height on ground-borne vibrations and providing a predictive model for vibration levels as a guideline for speed bump installation near sensitive structures. However, due to the complex nature of soil, which is difficult to approximate using ideal theoretical models or solve through numerical methods such as finite element analysis, data-driven end-to-end models present a more effective approach.

The Bornitz formula [18] is a classical model used to describe ground vibration propagation, which approximates the nonlinear behavior of soil by introducing geometric and material damping coefficients. However, the original form of the Bornitz formula is overly simplistic and does not accommodate the diverse needs of different site types. As a result, many researchers have calibrated and modified the Bornitz formula based on field test results. Kim & Lee [19] represented various types of vibration sources and their induced waves through geometric modeling, determining the geometric damping coefficients for different vibrations, which showed good agreement with field test results. Ren et al. [20] developed a vibration attenuation model in layered homogeneous media based on the Bornitz formula, providing an alternative tool to further investigate the impact of high-speed train-induced vibrations on foundation soils and adjacent underground structures. Niu et al. [21], building upon the Bornitz model and incorporating measured data, discussed the geometric attenuation and damping attenuation coefficients of the formula, using the optimized Bornitz model to predict ground vibrations caused by high-speed trains in loess areas. However, due to the limitations in the frequency range of field tests and the challenges in deriving the formula, research on frequency-dependent Bornitz models remains insufficient, failing to capture the elastoplastic characteristics of soil, such as resonance and absorption.

In recent years, the development of machine learning and artificial intelligence has introduced a new paradigm for addressing data-driven problems in the engineering field [22–24]. Many researchers have applied these technologies to the modeling and fitting of ground vibration propagation and attenuation patterns. Cao et al. [25] proposed a novel distance estimation algorithm for periodic surface vibrations, introducing a frequency band energy percentage feature and an enhanced computationally efficient k nearest neighborhood algorithm, demonstrating superior performance in distance prediction for earth surface periodic vibration signals. Monjezi et al. [26] proposed a prediction model for blast-induced ground vibration using artificial neural networks, demonstrating its superior accuracy compared to traditional empirical and statistical methods in predicting peak particle velocity based on parameters such as maximum charge per delay, distance from the blasting face, stemming, and hole depth. Liu et al. [27] proposed an efficient deep learning-based approach for identifying and analyzing train-induced ground-borne vibrations, utilizing a hybrid CNN-LSTM model and continuous wavelet transform for feature extraction, and investigates the uncertainty in vibration responses through long-term monitoring and statistical analysis. Verma & Singh [28] proposed a comparative study on the application of genetic algorithm optimization technique for predicting peak particle velocity in ground vibration, demonstrating its superior accuracy and robustness over traditional empirical equations and artificial neural networks in predicting ground vibration parameters based on blast design and explosive parameters. Although deep neural networks and other black-box models possess strong data fitting capabilities, their lack of physical interpretability raises concerns about their out-of-distribution generalization ability, particularly for problems with a strong physical basis, such as vibration propagation. This limitation makes it challenging to integrate these models with subsequent assessment tasks.

Beijing High Energy Photon Source (HEPS) is a major national scientific infrastructure located in the Huairou Science City, China. It is the country's first high-energy synchrotron light source capable of emitting extremely bright synchrotron radiation, with a brightness 10 trillion times greater than that of the sun. This makes HEPS a powerful tool for research in the microscopic world. Controlling the surrounding environmental vibrations of HEPS is crucial, as even minute vibrations can affect the stability of the electron beam, which in turn impacts the accuracy of experimental data. Ensuring a low-vibration environment is key to obtaining reliable scientific results. To assess the impact of ground vibrations induced by various environmental factors on HEPS, this paper combines the advantages of several methods previously discussed and, based on on-site experiments, proposes a hybrid iterative fitting approach for the propagation and attenuation law. This approach integrates the Bornitz formula with an intelligently generated model. The main contributions are as follows:

1. Field experiments were conducted at HEPS using a vibrator to generate sinusoidal excitation forces in the frequency range of 1–100 Hz. Displacement root mean square (RMS) values were calculated for all measurement points. To ensure data reliability, records with coherence values less than 0.9 were excluded from subsequent analyses.

2. Combining traditional machine learning methods with formula generation intelligent models to discover propagation and attenuation laws based on the Bornitz model, leading to the development of a ground vibration propagation formula that is frequency-dependent.

3. Employing probabilistic analysis methods to estimate the error range of the fitting formula and providing an explanation of the physical rationality of the formula based on theoretical derivation and numerical simulation.

4. Comparing the proposed method with black-box machine learning models and previous empirical

formulas, demonstrating its significant advantages in terms of accuracy and interpretability.

The organization of the remaining sections of the paper is as follows. Section 2 details the on-site experiment and data processing methods. Section 3 presents the hybrid iterative fitting approach for the attenuation law based on the Bornitz formula and formula generation intelligent models, along with the process of formula discovery, error analysis, and interpretation of the physical rationality. Section 4 compares the proposed formula with previous empirical formulas and the fitting results of black-box machine learning models. Section 5 provides a conclusion of the paper.

2. Experiment and Data processing



Fig. 1 The layout of HEPS site

The High Energy Photon Source (HEPS), as shown in **Fig. 1**, is the first fourth-generation synchrotron light source facility being built in China [29]. Located in the northern core area of Huairou Science City in Beijing, this advanced facility serves as a high-performance, high-energy synchrotron radiation light source. Its high luminosity design demands stringent beam stability, which in turn

requires precise control over surrounding vibrations. Consequently, it is crucial to investigate the vibration attenuation and propagation characteristics at the HEPS site to evaluate the impact of ground vibrations on the facility's performance.

2.1. Testing device



(a) Vibration test sensor



(b) On-site consistency test for the sensor

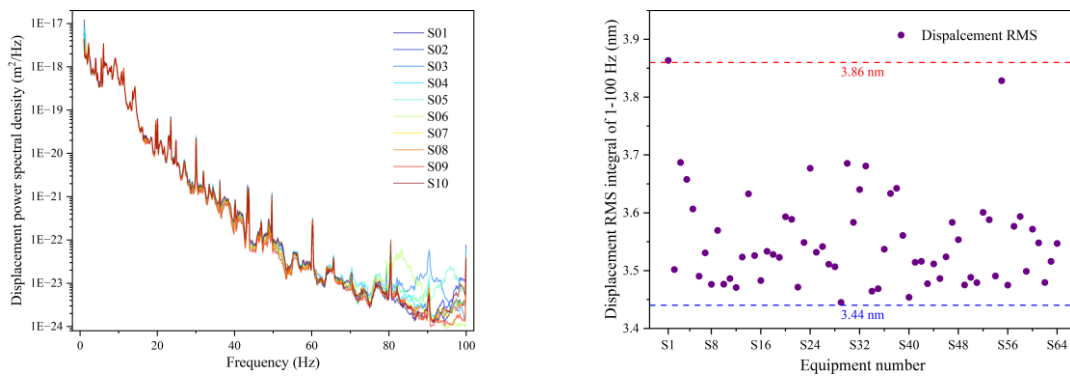
Fig. 2 The sensor employed for testing and the on-site consistency test of the sensor on the HEPS experimental hall slab.

The vibration sensors used in this experiment were the Smartsolo IGU-16HR 3C AIO, a three-component velocimeter manufactured by Shenzhen Mianyuan Intelligent Technology Co., Ltd as shown in **Fig. 2 (a)** [30]. These instruments have a frequency range of 0.2 Hz to 1000 Hz and a sensitivity of 76.7 V/m/s. Prior to testing, the consistency of all the sensors was verified on the slab of the HEPS experimental hall. The on-site test setup is depicted in **Fig. 2(b)**. Random noise measurements were taken at midnight, and one hour of data was selected for consistent comparison, with a frequency resolution of 0.1 Hz. The displacement Root Mean Square (RMS) values, within the frequency range of 1-100 Hz, for all the sensors were calculated in the frequency domain using Equation (1) [31]:

$$x_{RMS}(f_1, f_2) = \sqrt{\sum_{f_1}^{f_2} S_x(f) \Delta f} = \sqrt{\sum_{f_1}^{f_2} \frac{S_v(f)}{(2\pi f)^2} \Delta f} \quad (1)$$

Where S_x and S_v are the displacement and velocity Power Spectrum Density (PSD) respectively, f is the vibration frequency, f_1 and f_2 are the starting frequency and cutting frequency respectively considered, Δf is the frequency resolution.

The comparative results of the displacement PSD for instruments S01 to S10 are illustrated in **Fig. 3 (a)**. All others sensors give similar results. The results demonstrate excellent consistency below 50 Hz across all sensors. The differences observed in the 50 Hz–100 Hz frequency range are primarily due to variations in the self-noise characteristics of the sensors. As shown in **Fig. 3(b)**, the dispersion of the displacement RMS integral over the 1-100 Hz range for 64 units is within 0.5 nm. Furthermore, the comparison of the displacement RMS integral across the frequency range of 1-100 Hz for all 50 sensors also reveals excellent consistency, with a dispersion of within 0.5 nm.



(a) Displacement PSD comparison of S01 to S10 (b) The RMS distinguishes of all 64 sensors

Fig. 3 Comparison of Displacement PSDs (S01–S10) and RMS Variability Across 64 Sensors

2.2. Field test arrangement



(a) The test location and the measurement line (b) Vibration exciter

Fig. 4 The artificial vibration exciter and the excitation test location.

Vibration attenuation measurements were conducted on the bare ground within the HEPS storage ring,

as shown in **Fig. 4(a)**. The measurement line, marked in red, has a total length of 336 meters, with 64 measurement devices (labeled S1–S64) distributed along this line. The first 50 points are spaced approximately one meter apart to capture more detailed attenuation characteristics. Beyond this, the spacing gradually increases, ranging from about 10 meters to 100 meters, 20 meters to 200 meters, and 50 meters to 336 meters.

To generate unique vibration frequency, an artificial exciter was used. The shaker utilized in this study, shown in **Fig. 4 (b)**, is manufactured by Suzhou Dongling Vibration Testing Instrument Co. [32]. This shaker, with a total mass of 1 ton, generates wide-band vibrations from 1 Hz to 100 Hz. However, due to the limited maximum displacement of the shaker's moving coil during excitation, the vibration amplitude below 10 Hz cannot be set to a large amplitude. Despite this limitation, the signal-to-noise ratio remains favorable in the 10–100 Hz frequency range, even at a distance of 400 meters from the vibration source. This effectively mitigates the limitations associated with traditional artificial vibration sources, such as traffic loads and environmental noise.

2.3. Data processing

The shaker generated vertical sinusoidal excitation forces ranging from 1 Hz to 100 Hz in 1 Hz increments, with each frequency lasting for 40 seconds. To mitigate interference from human activities, all tests were performed during midnight from 1am to 4am under low-ambient-noise conditions. During continuous excitation, the excitation frequency was altered every 40 seconds, with varying vibration amplitudes across frequencies. Transient amplitude fluctuations (1–2 seconds) occurred during frequency transitions. To minimize interference from these transients, the first 5 seconds and the last 5 seconds of data for each frequency interval were discarded in subsequent calculations. The intermediate 30-second stable segment was retained for analysis.

Although the vibration signal-to-noise ratio is generally high, certain measurement points at specific frequencies exhibit weak coherence with the initial testing point. In this study, the coherence between the signals from each sensor and the first sensor, ranging from S02 to S64, is calculated. Data with a coherence value below 0.9 are excluded. The calculation formula is as follows:

$$\gamma = \frac{|P_{xy}|^2}{P_{xx}P_{yy}} \quad (2)$$

Where P_{xx} and P_{yy} represent the auto power spectral densities of signal x and signal y , respectively; P_{xy} denotes the cross power spectral density between signal x and signal y ; and γ represents the coherence.

Fig. 5 illustrates the coherence analysis for the last five measurement points of S59–S64. Data with coherence coefficients below the threshold of 0.9, observed at specific frequency intervals, were excluded in subsequent computational analysis to ensure fitting reliability.

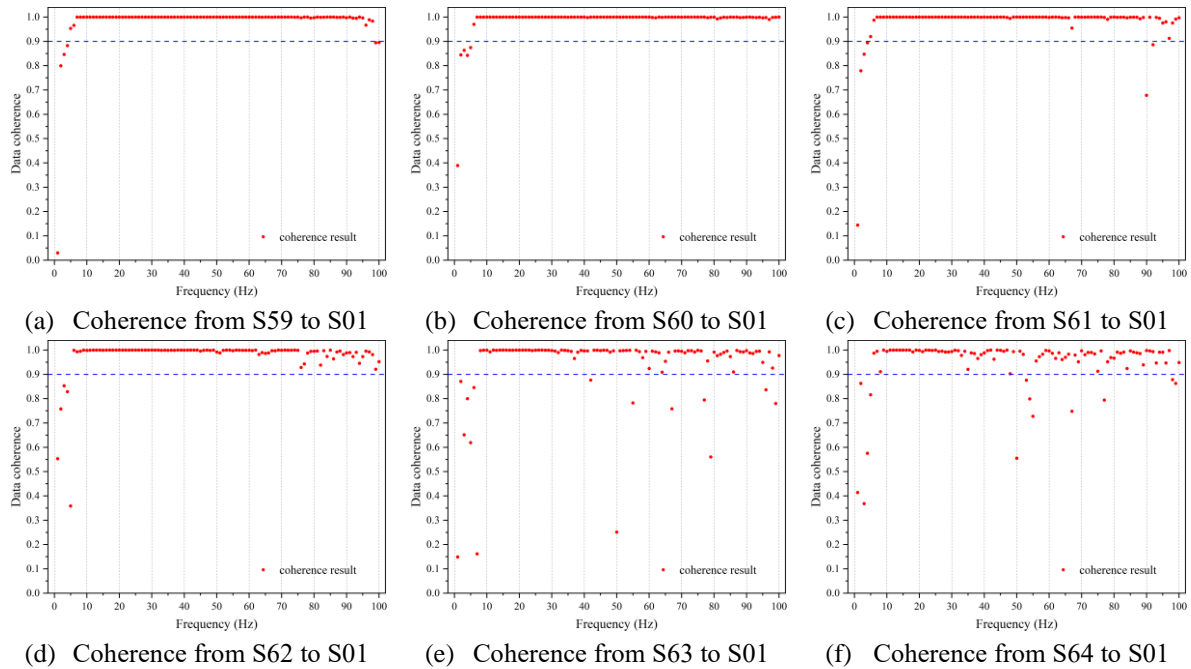


Fig. 5 The coherence analysis for the last five measurement points of S59–S64

3. Propagation and Attenuation Law Discovery

3.1. Method

The propagation and attenuation of ground vibrations are influenced by various factors, including the amplitude of the vibration source, propagation distance, and soil properties. For a given vibration, the energy attenuation during propagation—manifested as amplitude decay—is primarily governed by two key factors: geometric and material attenuation. This process is well described by the Bornitz equation [18]:

$$A_r = A_0 \left(\frac{r_0}{r} \right)^n e^{-\alpha(r-r_0)} \quad (3)$$

where A_0 and r_0 represent the amplitude and distance from the vibration source at the reference point, while A_1 and r_1 denote the amplitude and distance from the source at the calculation point. The parameters n and α correspond to the geometric damping coefficient and material damping coefficient, respectively. As a fundamental equation describing the attenuation law, the Bornitz equation is independent of the choice of the reference point, ensuring that the following three relationships remain consistently valid for any r_0 , r_1 and r_2 :

$$A_{r_1} = A_0 \left(\frac{r_0}{r_1} \right)^n e^{-\alpha(r_1-r_0)} \quad (4)$$

$$A_{r_2} = A_0 \left(\frac{r_0}{r_2} \right)^n e^{-\alpha(r_2-r_0)} \quad (5)$$

$$A_{r_2} = A_{r_1} \left(\frac{r_1}{r_2} \right)^n e^{-\alpha(r_2-r_1)} \quad (6)$$

This self-consistency arises from the inherent properties of power functions and exponential functions, which also reinforce the physical significance of the Bornitz equation. To account for the influence of frequency on vibration propagation and attenuation while maintaining this self-consistency, we treat the geometric damping coefficient n and the material damping coefficient α as functions of frequency f .

Consequently, we derive the functional form to be fitted as follows:

$$A_r = A_0 \left(\frac{r_0}{r} \right)^{n(f)} e^{-\alpha(f)(r-r_0)} \quad (7)$$

For the unknown functional forms of $n(f)$ and $\alpha(f)$, traditional methods based on polynomial fitting and the least squares approach are often inefficient and heavily reliant on expert experience. These methods tend to perform poorly when dealing with large datasets, leading to suboptimal fitting results. In recent years, with the advancement of generative artificial intelligence, research on its application to formula discovery tasks has been steadily emerging, leading to the development of intelligent models for formula generation [33–35]. These formula generation models represent mathematical expressions in the form of prefix notation. For example, the expression $a \times (b + c)$ is rewritten as $\times a + b c$, thereby eliminating the need for parentheses. This transformation converts a formula into a sequence composed solely of "tokens", including operators and variables, which can then be processed by generative artificial intelligence models such as Long Short-Term Memory (LSTM) networks [36] and Transformer architectures [37]. Chen et al. [38] integrated feature engineering with intelligent formula generation models, significantly enhancing the model's representational capacity. This advancement enables the generation of physically meaningful, dimensionally consistent piecewise function formulas and facilitates the handling of complex engineering problems.

However, intelligent formula generation models face computational efficiency challenges when dealing with large-scale data. Moreover, they are not well-suited for formula discovery tasks of the form given in Equation (7), where part of the equation is fixed while the other part requires fitting. To address these limitations, we build upon the model proposed by Chen et al. [38] and introduce a hybrid iterative fitting approach that integrates traditional machine learning with intelligent formula generation models, specifically designed for the formula discovery task in Equation (7). For a given frequency f , a simple transformation of Equation (7) yields the following relationship:

$$n(f) \log\left(\frac{r_0}{r}\right) = \log\left(\frac{A_r}{A_0}\right) + \alpha(f)(r - r_0) \quad (8)$$

$$\alpha(f)(r - r_0) = n(f) \log\left(\frac{r_0}{r}\right) - \log\left(\frac{A_r}{A_0}\right) \quad (9)$$

In other words, if α (or n) is treated as a constant, determining n (or α) at a specific frequency f can be formulated as a linear fitting problem without bias. This type of problem can be described as follows: Given a set of data points $\{(x_1, y_1), (x_2, y_2), \dots, (x_n, y_n)\}$, the goal is to find the optimal k such that the fitting relationship $kx = y$ minimizes the squared error. Through a straightforward derivation, it can be obtained that:

$$k = \frac{\sum_{i=1}^n x_i y_i}{\sum_{i=1}^n x_i^2} \quad (10)$$

Thus, without altering the values of $\alpha(f)$ (or $n(f)$), we can determine the optimal n (or α) for each frequency f that minimizes the fitting error. Next, we employ the intelligent formula generation model to identify the functional relationship $n(f)$ (or $\alpha(f)$). We then reverse the process, fixing the obtained $n(f)$ (or $\alpha(f)$) and repeating the same procedure to derive a new functional relationship for $\alpha(f)$ (or $n(f)$). Through iterative refinement, the formula's fitting error gradually decreases, ultimately yielding a highly accurate fitted expression. Starting with $n(f) = 0$ as the initial condition, the workflow of our method is illustrated in Fig. 6.

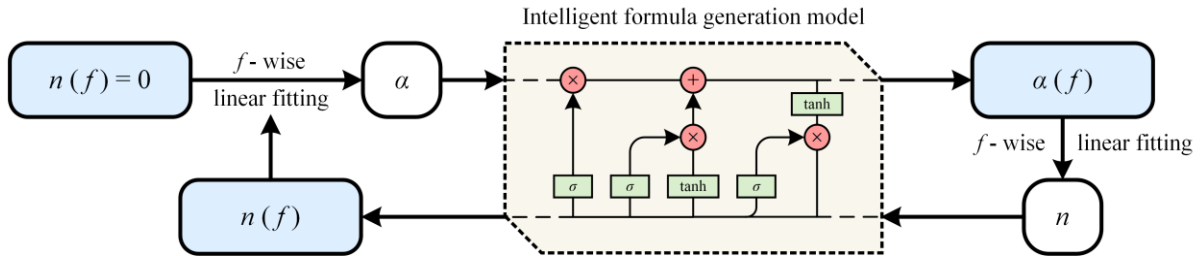


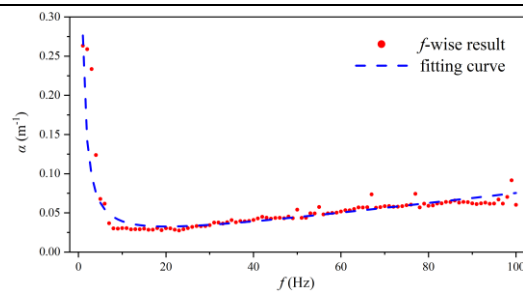
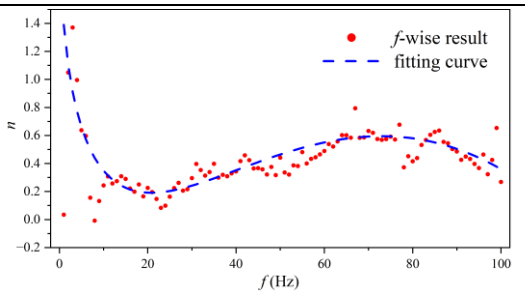
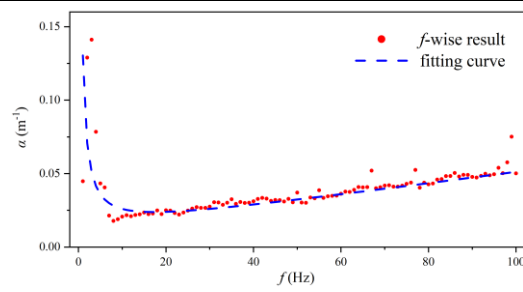
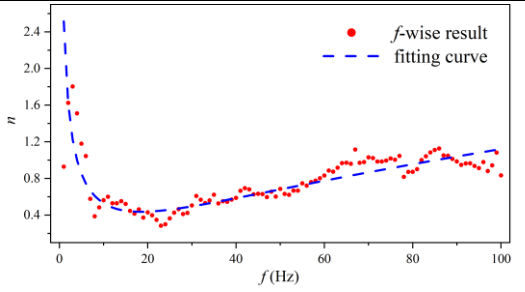
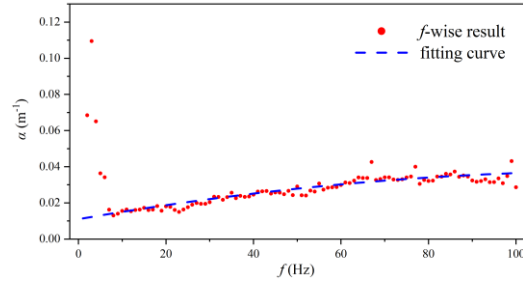
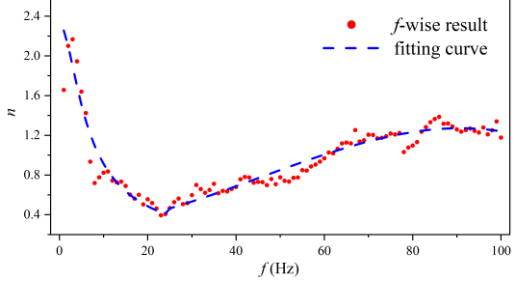
Fig. 6 The workflow of our formula discovery method

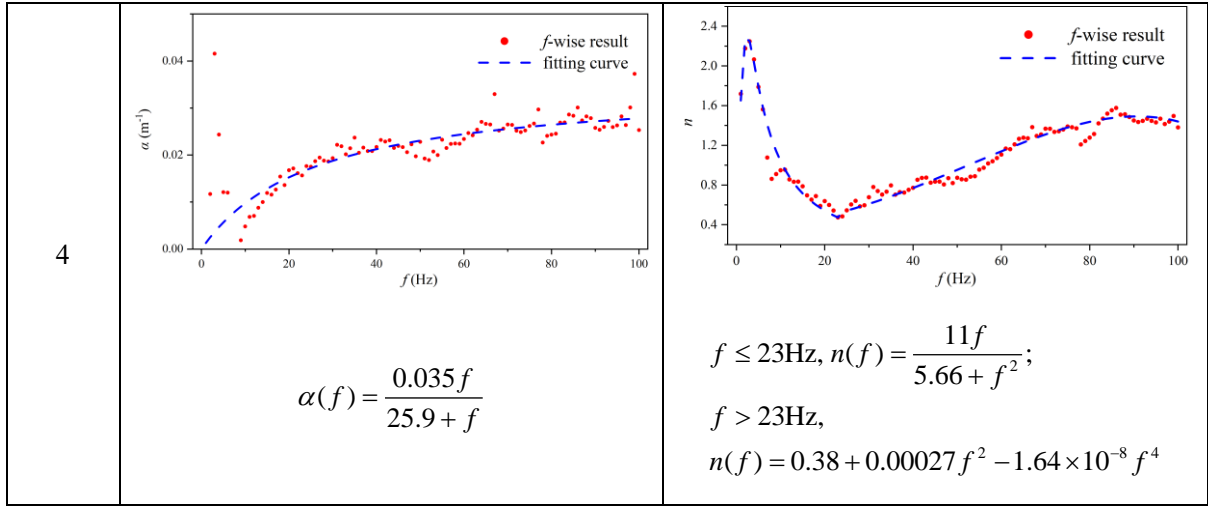
3.2. Formula discovery

Select the measuring point $r_0 = 2.1\text{m}$, which is the closest to the vibration source, as the reference point.

With $n(f) = 0$ as the initial condition, the functional expressions of material damping coefficient $\alpha(f)$ and geometric damping coefficient $n(f)$ are iterated for 4 rounds according to the process shown in **Fig. 6**. The fitting results of each round are presented in **Table 1**.

Table 1 The process of formula discovery

Round	Material Damping Coefficient $\alpha(f)$	Geometric Damping Coefficient $n(f)$
1	 $\alpha(f) = 0.0057 + 0.0067f + \frac{0.27}{f}$	 $n(f) = 2.26 + 0.13f - \sqrt{f} - 0.00049f^2$
2	 $\alpha(f) = 0.01 + 0.0004f + \frac{0.12}{f}$	 $n(f) = \sqrt{0.028f + \frac{9.55}{f}} - 0.581$
3	 $\alpha(f) = 0.011 + 0.00042f - 1.65 \times 10^{-6} f^2$	 $f \leq 24\text{Hz}, n(f) = \sqrt{\frac{98.7}{18.4 + f^2}};$ $f > 24\text{Hz},$ $n(f) = 0.28 + 0.00036f^2 - 2.64 \times 10^{-6} f^3$



The fitting results of each iteration are substituted into Equation (7) to calculate the mean absolute error (MAE) and relative mean absolute error (RMAE) of the formula, as shown in **Fig. 7**. It can be observed that the iterative fitting process of the formula significantly reduces the fitting error. Moreover, as shown in **Table 1**, the intelligent formula generation model is capable of identifying formula forms that go beyond conventional empirical knowledge. This approach combines the powerful fitting ability of deep learning with the simplicity and intuitiveness of formulas, thereby providing a strong guarantee for the accuracy and interpretability of the model.

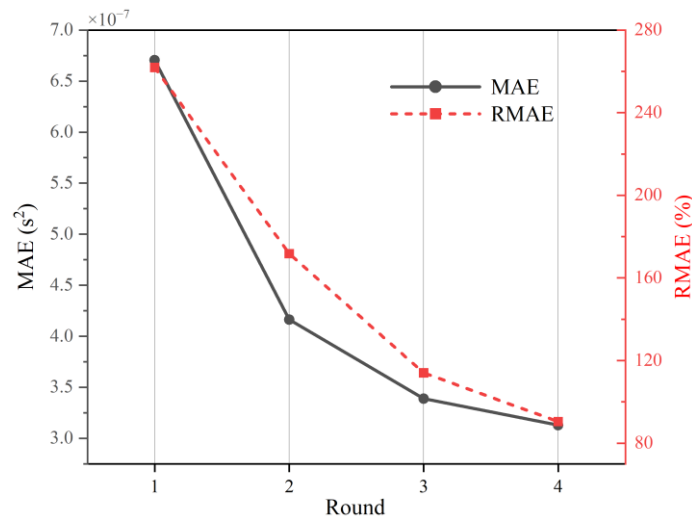


Fig. 7 Error reduction during the iterative process

3.3. Error analysis

Based on the formula discovered in Section 3.2, the equation for determining the propagation and

attenuation of ground vibration is as follows:

$$A_r = A_0 \left(\frac{r_0}{r} \right)^{n(f)} e^{-\alpha(f)(r-r_0)} \quad (11)$$

$$n(f) = \begin{cases} \frac{11f}{5.66 + f^2}, f \leq 23\text{Hz} \\ 0.38 + 0.00027f^2 - 1.64 \times 10^{-8} f^4, f > 23\text{Hz} \end{cases} \quad (12)$$

$$\alpha(f) = \frac{0.035f}{25.9 + f} \quad (13)$$

where the MAE is $3.13 \times 10^{-7} \text{ s}^2$ and the RMAE is 90.47%. Owing to the varying initial amplitudes of the vibration sources at different frequencies and the order-of-magnitude differences arising from the attenuation of vibrations with distance, the MAE, when measured in absolute terms, fails to adequately reflect the fitting error of the formula. Additionally, the complex nature of soil and the small measured true values at greater distances lead to an overestimation of the relative error. Consequently, the RMAE alone cannot intuitively represent the fitting performance of the formula. **Fig. 8** presents the cumulative distribution curve of the relative errors, where the x-axis represents the relative error, and the y-axis indicates the proportion of data points with a relative error less than or equal to the corresponding value out of the total number of data points. It can be observed that 36.5% of the data points have a relative error of less than 30%, 56.4% have a relative error of less than 50%, and 81.0% have a relative error of less than 100%. Additionally, 90.9% of the data points exhibit a relative error within 200%. Such precision is remarkably high for the fitting of soil problems, thereby demonstrating the effectiveness of our proposed method and formula. To further investigate whether the data points with relative errors exceeding 200% are due to the complex environmental conditions or to the inadequate fitting of the model at specific measurement points under certain frequencies, **Fig. 9** presents a distribution map of the data points with relative errors greater than 200%. It can be observed that the distribution of these data points does not exhibit any clear pattern (the concentration of these points in the lower range of r is due to the fact that the measurement points are

predominantly located in the lower range of r). This finding demonstrates the robust generalization capability of the formula within the tested range.

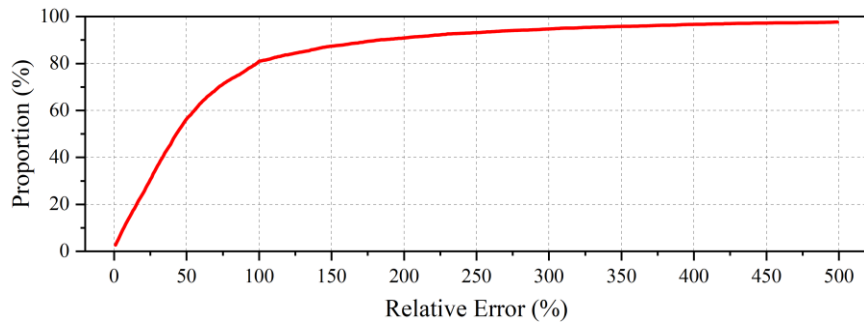


Fig. 8 Cumulative distribution curve of the relative errors

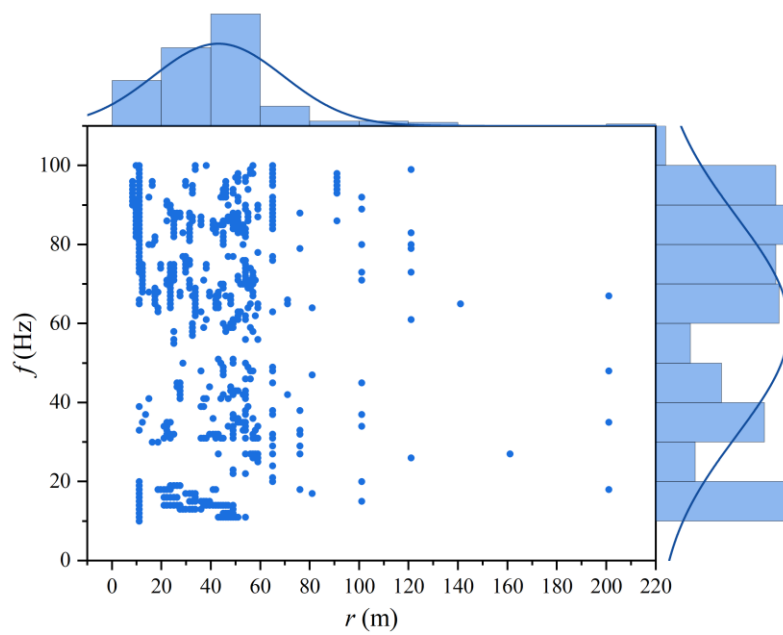


Fig. 9 Distribution map of the data points with relative errors greater than 200%

Given the complex influence of environmental factors and the discrete nature of soil, the propagation and attenuation of ground vibration exhibit a certain degree of randomness. A single formula is insufficient to accurately assess their impacts. Assuming that the true amplitude A_r at a distance r from the vibration source and the predicted amplitude \tilde{A}_r from the formula follow a f -independent probability distribution, the model can be calibrated using measurement results across different frequencies. The following three hypotheses were made regarding this probability distribution:

1. $A_r - \tilde{A}_r$ follows a normal distribution $\mathcal{N}(\mu, \sigma^2)$
2. A_r / \tilde{A}_r follows a normal distribution $\mathcal{N}(\mu, \sigma^2)$
3. A_r / \tilde{A}_r follows a log-normal distribution $\mathcal{LN}(\mu, \sigma^2)$, or equivalently, $\log(A_r / \tilde{A}_r)$ follows a normal distribution $\mathcal{N}(\mu, \sigma^2)$

The Shapiro-Wilk (SW) test is a widely used statistical method for assessing whether a dataset follows a normal distribution. It evaluates the null hypothesis (H_0) that the data originate from a normally distributed population. The test computes a test statistic W , which measures the extent to which the data conform to a normal distribution. The W statistic is defined as:

$$W = \frac{\left(\sum_{i=1}^n a_i x_i\right)^2}{\sum_{i=1}^n (x_i - \bar{x})^2} \quad (14)$$

where x_i represents the ordered sample values, \bar{x} is the sample mean, and a_i are constants derived from the expected values of order statistics from a standard normal distribution. The value of W lies between 0 and 1, with values closer to 1 indicating a stronger conformity to normality. For comparative analysis, the W statistic can be used to rank multiple datasets based on their degree of normality. A higher W value suggests that the dataset more closely follows a normal distribution. Unlike the p-value, which only provides a binary decision regarding normality at a given significance level, the W statistic allows for relative comparisons among different distributions. This makes it particularly useful in evaluating which dataset exhibits greater adherence to normality, especially in small-sample scenarios where other normality tests may be less reliable. Perform the SW test for each r under the three aforementioned hypotheses and compute the corresponding W values. The results are shown in **Fig. 10**.

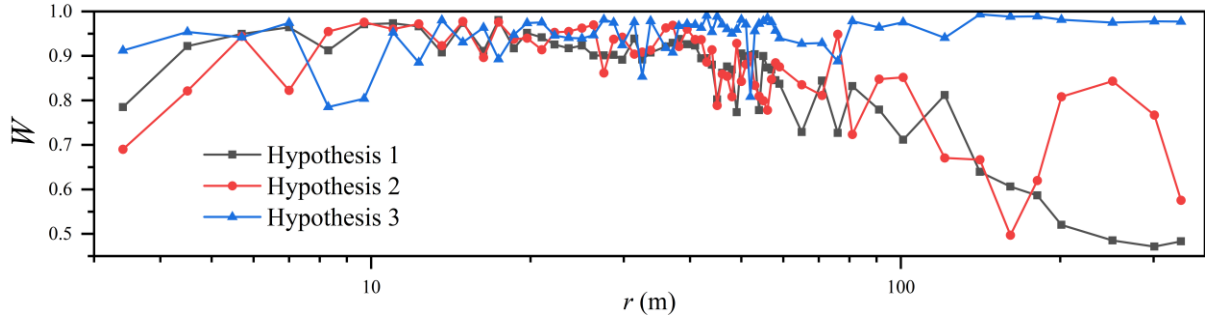


Fig. 10 W value for each r under the three hypotheses

It can be observed that the overall W values for Hypothesis 3 are higher, indicating that the assumption that $\log(A_r / \tilde{A}_r)$ follows a normal distribution is more reasonable. Building on this, for each r , we assume $\mu = 0$ and use data from different f values to obtain an unbiased estimate of σ , as shown in **Fig. 11**. Subsequently, the intelligent formula generation model is employed to fit the functional relationship between σ and r , expressed as follows:

$$\sigma = \frac{0.62}{1 - 0.0025r} \quad (15)$$

Based on the fitted results, the 1-2-3- σ range for different r values is determined, as illustrated in **Fig. 12**. The results show that 71.5% of the data points fall within the 1- σ range, 94.2% of the data points fall within the 2- σ range, and 98.7% of the data points fall within the 3- σ range, demonstrating the effectiveness of the fitting model.

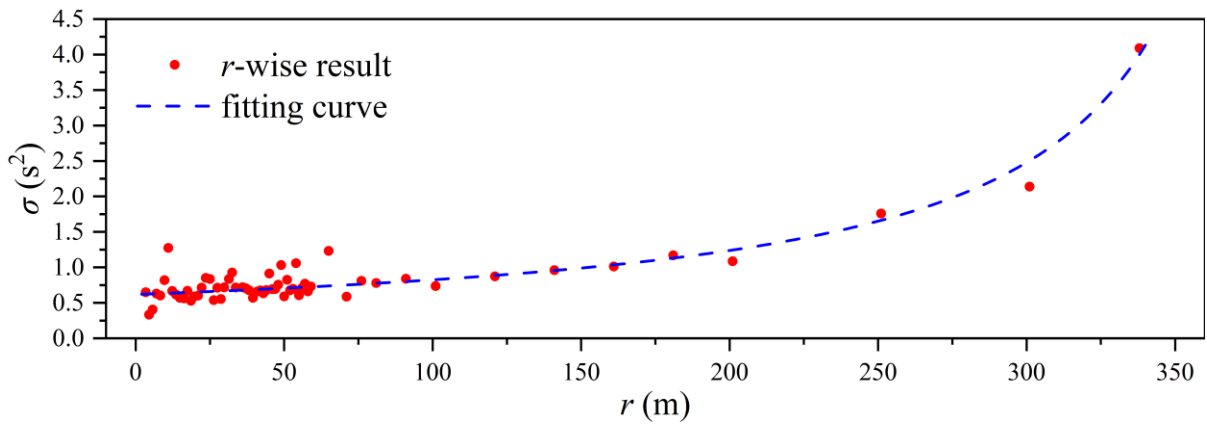


Fig. 11 Estimate of σ for each r

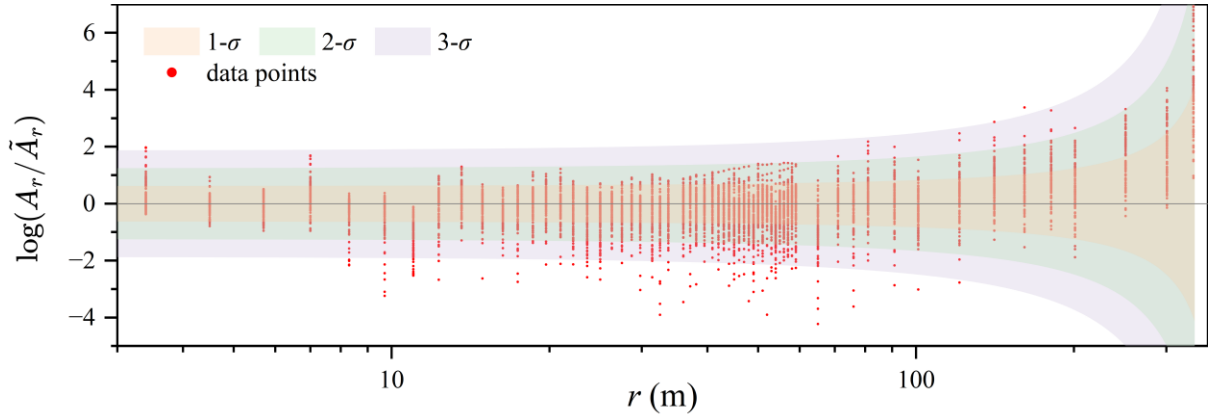


Fig. 12 Error band for each r

3.4. Physically interpretation

In the Bornitz formula, the geometric damping coefficient n is considered to be related to the spatial diffusion of wave energy, while the material damping coefficient α is associated with the absorption of wave energy by the soil. The material damping coefficient α is influenced by the complex properties of the soil, making it challenging to establish a universal physical interpretation. The study by Yang [39,40] suggests a positive correlation between the material damping coefficient α and frequency f , which aligns with the form of our equation. However, the relationship between the geometric damping coefficient n and frequency f has received relatively little attention in existing research.

The energy density of a wave is proportional to the square of its amplitude. Under ideal conditions, a point source in three-dimensional space emits waves that propagate spherically. According to the law of energy conservation, the total energy across different spherical surfaces must remain constant. Consequently, the energy density is inversely proportional to the square of the distance r from the source, leading to the conclusion that the amplitude A is inversely proportional to r :

$$A \propto r^{-1} \quad (16)$$

Similarly, for a point source emitting waves in a two-dimensional plane, the amplitude A should be inversely proportional to $r^{0.5}$:

$$A \propto r^{-0.5} \quad (17)$$

Given the assumption that all energy on one plane is instantaneously transferred to the next, while in reality, only a portion of the energy is transmitted, the actual energy transfer is likely to be lower. Therefore, for ground vibrations that couple planar and spatial wave propagation, the geometric damping coefficient n should be no less than 0.5. In our proposed Equation (12), the minimum value of the geometric damping coefficient n is 0.47, which is consistent with the theoretical derivation mentioned above.

Without considering material damping, in an isotropic, homogeneous elastic medium, the displacement field $\mathbf{u}(\mathbf{x}, t)$ satisfies the elastodynamic equation:

$$\rho \frac{\partial^2 \mathbf{u}}{\partial t^2} = (\lambda + 2\mu)\nabla(\nabla \cdot \mathbf{u}) - \mu\nabla \times (\nabla \times \mathbf{u}) \quad (18)$$

where ρ is the mass density, λ and μ are Lamé parameters characterizing the elastic properties of the medium.

To investigate the relationship between geometric damping coefficient n and f or r , we employ the ABAQUS/Explicit solver, which is well-suited for transient dynamic analysis involving wave propagation.

The explicit time integration scheme efficiently handles the high-frequency components of the elastic waves and ensures stable numerical simulations. As shown in **Fig.13**, we establish a $500\text{m} \times 500\text{m} \times 500\text{m}$ elastic solid domain to simulate the propagation of vibrations generated by a point source on the ground surface.

The material properties are set as follows: density 1500 kg/m^3 , Young's modulus 5000 kPa , and Poisson's ratio 0.4 . A sinusoidal pulse with frequencies $f = 1 \text{ Hz}$, 5 Hz , 10 Hz , and 20 Hz is applied at the source location, and the maximum amplitude A_m at points in the horizontal observation direction is recorded. By analyzing the slope k of the $\log(A_m) - \log(r)$ curve, the geometric damping coefficient n for each frequency is determined, as illustrated in **Fig.14**.

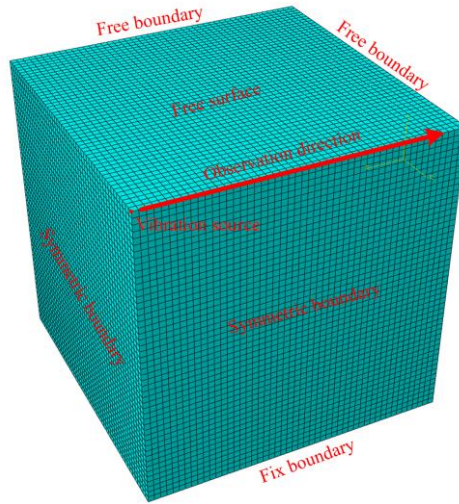


Fig. 13 ABAQUS/Explicit modeling

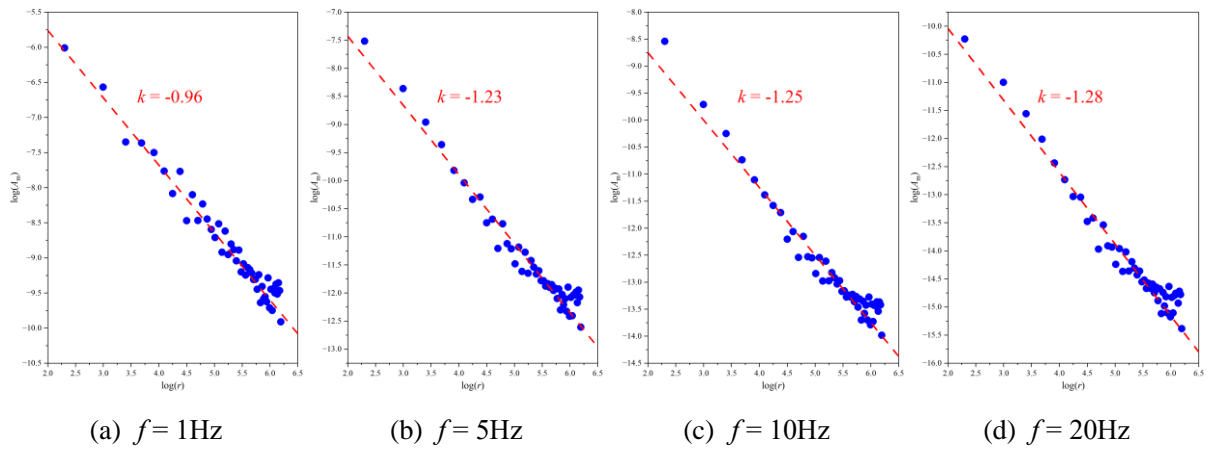


Fig. 14 Simulation results

The results indicate that the $\log(A_m) - \log(r)$ relationship is nearly a straight line for all tested frequencies, confirming that the geometric attenuation coefficient n remains independent of distance r . This supports our assumption that the geometric damping coefficient n depends only on frequency. Furthermore, the geometric damping coefficient exhibits an increasing trend with frequency, which is consistent with the second term in our proposed Equation (12). However, due to the complex and discrete nature of soil, accurately replicating its behavior in numerical simulations remains challenging. As a result, while our numerical simulations provide validation for the general form of our equation, the specific values of the geometric damping coefficients obtained from the simulations do not carry direct physical significance.

4. Discussion

To verify the accuracy of the proposed formula in this study, we compare its performance with previously established formulas and the fitting results of black-box machine learning models. Regarding the previously proposed formulas, the first one is the original Bornitz formula, which does not consider the influence of frequency:

$$A_r = A_0 \left(\frac{r_0}{r} \right)^n e^{-\alpha(r-r_0)} \quad (19)$$

This formula requires the calibration of the geometric damping coefficient n and the material damping coefficient α . The second is the frequency-dependent Bornitz formula developed by Yang [40] through theoretical derivation and experimental validation:

$$A_r = A_0 \sqrt{\frac{r_0}{r} [1 - \xi(1 - \frac{r_0}{r})]} e^{-\alpha f(r-r_0)} \quad (20)$$

which requires the calibration of the site coefficient ξ and the material damping coefficient α . The parameter calibration for both formulas is conducted using the *scipy.optimize.minimize* function [41] in Python library, aiming to minimize the mean absolute error (MAE). The final calibration results are as follows:

$$A_r = A_0 \left(\frac{r_0}{r} \right)^{0.885} e^{-0.071(r-r_0)} \quad (21)$$

$$A_r = A_0 \sqrt{\frac{r_0}{r} [1 - 0.865(1 - \frac{r_0}{r})]} e^{-0.001f(r-r_0)} \quad (22)$$

Regarding black-box machine learning models, we selected two powerful fitting techniques: the traditional gradient boosting model Extreme Gradient Boosting (XGboost) and the recently emerging deep neural network (DNN). XGBoost is an efficient and scalable implementation of gradient boosting that has been widely used in regression and classification tasks. It builds an ensemble of decision trees sequentially, optimizing the model by minimizing a specified loss function while incorporating regularization to prevent

overfitting. XGBoost is particularly well-suited for structured data and has demonstrated strong generalization capabilities across various domains. DNN is a class of artificial neural networks that consist of multiple hidden layers, enabling them to capture complex nonlinear relationships in data. Unlike traditional machine learning models, DNN leverages deep hierarchical feature extraction, making them highly effective for tasks requiring high-dimensional representations. In this study, we employ a feedforward DNN architecture trained using backpropagation and stochastic gradient descent. For the sake of fairness, similar to the formulas, both XGBoost and DNN take A_0 , r_0 , r , and f as inputs, with A_r as the output, employing MAE as the objective or loss function. Additionally, 75% of the data is used for training, and both the input and output variables are normalized using min-max scaling. In the experiment, the XGBoost is implemented with a maximum tree depth of 3, a learning rate of 0.1, and both the subsample ratio and column sampling ratio set to 0.8 to prevent overfitting. The model is trained for 1000 boosting rounds using the training dataset. The DNN consists of four hidden layers, each with 32 neurons, utilizing the sigmoid activation function. The model is optimized using the Adam optimizer with an initial learning rate of 0.01 and is trained for 10000 epochs.

To compare the accuracy of different methods in fitting the data, the results are presented in **Table 1**. It can be observed that the proposed formula achieves the lowest MAE and RMAE among all formula-based models. In contrast, the black-box machine learning models, XGBoost and DNN, exhibit lower MAE values, which is consistent with their strong fitting capabilities. However, both models have significantly higher RMAE values compared to the formula-based approach, indicating that their predictions are more susceptible to the influence of extreme values. However, as analyzed in **Section 3.3**, MAE and RMAE alone are insufficient to comprehensively evaluate the effectiveness of data fitting. To provide further insight, **Fig. 15** illustrates the cumulative distribution curves of relative errors for different methods. It can be observed

that the proposed formula exhibits a significant advantage over previous formulas within the range of relative errors below 100%, achieving a fitting accuracy comparable to that of black-box models. Additionally, the cumulative distribution curves of Bornitz's and Yang's formulas show a sudden increase at the 100% mark. This indicates that their predicted values are often significantly lower than the actual values, leading to a large number of points with relative errors close to 100%. This phenomenon is further confirmed in **Fig. 16**, which presents the distribution of the ratio between predicted \tilde{A}_r and actual values A_r for different methods. **Fig. 16** also reveals that some of the predicted values from XGBoost and DNN are negative, which is physically unrealistic. This further highlights the issue of low interpretability in black-box models, which becomes particularly pronounced in physics-related problems. Considering various evaluation criteria, our proposed method effectively integrates the strong fitting capability of black-box models with the simplicity and intuitiveness of analytical formulas. The discovered formula strikes a balance between accuracy and interpretability, demonstrating significant practical value for ground vibration prediction.

Table 1 Comparison of fitting accuracy of different methods

Method	MAE ($\times 10^{-7} \text{s}^2$)	RMAE (%)
Proposed	3.13	90.47
Bornitz's	4.16	99.26
Yang's	3.69	186.08
XGboost	1.25	567.90
DNN	1.74	701.52

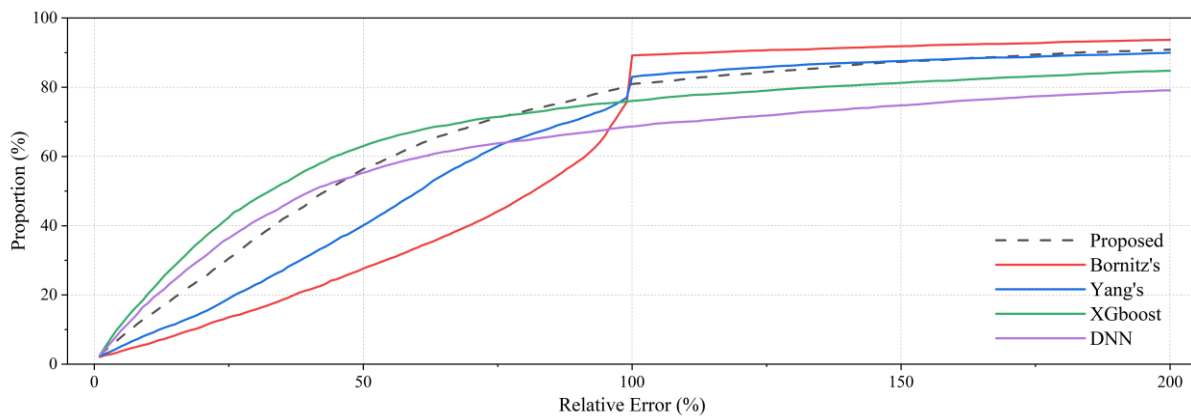


Fig. 15 Cumulative distribution curve of the relative errors for different methods

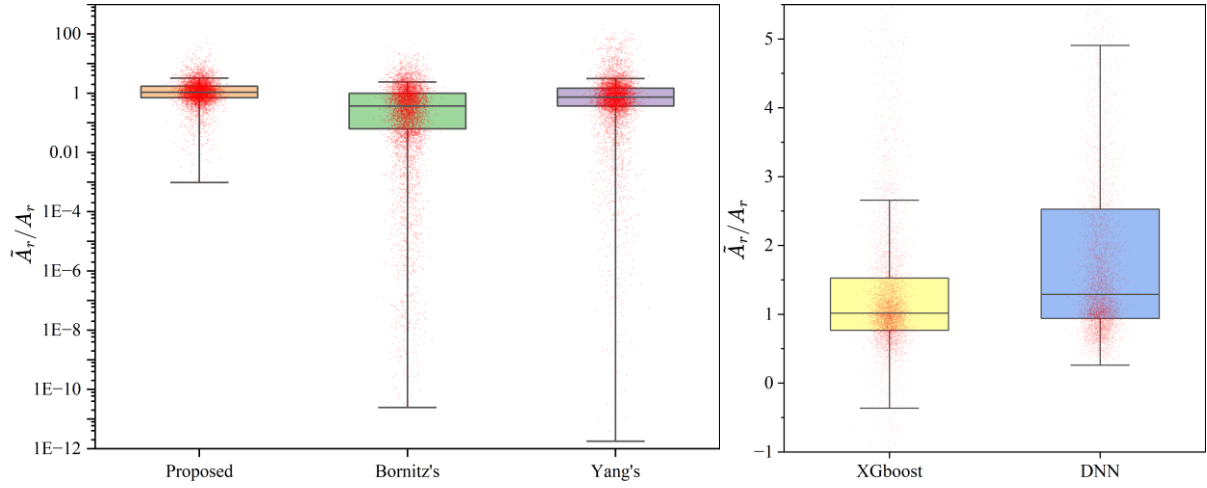


Fig. 16 Distribution of the ratio between predicted and actual values for different methods

5. Conclusions

In this study, we conducted ground vibration measurement experiments at the HEPS site in Beijing and employed intelligent methods to derive formulas describing the propagation and attenuation of vibrations. The main contributions of this work are summarized as follows:

1. High-fidelity vibration experiments are presented at the HEPS site, providing reliable data for understanding ground vibration propagation. The results lay a solid foundation for evaluating vibration impacts on precision instruments.
2. A formula discovery method integrating traditional machine learning techniques with intelligent formula generation models was proposed. This approach enables the efficient and rapid derivation of propagation and attenuation formulas based on the Bornitz model.
3. A probabilistic model was employed to analyze the errors of the discovered formulas, providing a bounded error range model. Additionally, theoretical analysis and numerical modeling were conducted to validate the rationality of the proposed formula structure.
4. A comparative analysis was performed against previously proposed formulas and black-box models, demonstrating that the proposed method achieves both high accuracy and

interpretability, making it suitable for ground vibration prediction and assessment.

This research offers a practical and scalable methodology for quantitatively evaluating the impact of environmental vibrations—such as those induced by traffic, construction, or natural events—on high-precision scientific infrastructure. The derived propagation formulas, with both physical interpretability and predictive accuracy, hold great promise for supporting the design, operation, and vibration control strategies of next-generation ultra-sensitive facilities, including synchrotron light sources, quantum laboratories, and gravitational wave observatories.

6. Acknowledgements

The authors gratefully acknowledge the financial support provided by the General Program of National Natural Science Foundation of China, under fund approval No. of 12375150.

7. References

- [1] Q. Jin, D.J. Thompson, D.E.J. Lurcock, E. Ntotsios, The shadow effect on the ground surface due to vibration transmission from a railway tunnel, *Transportation Geotechnics* 23 (2020) 100335. <https://doi.org/10.1016/j.trgeo.2020.100335>.
- [2] X. Zhang, S. Zhou, C. He, H. Di, J. Si, Experimental investigation on train-induced vibration of the ground railway embankment and under-crossing subway tunnels, *Transportation Geotechnics* 26 (2021) 100422. <https://doi.org/10.1016/j.trgeo.2020.100422>.
- [3] H. Zhang, M. Qin, K. Liao, K. Wang, G. He, Pipe-soil vibration characteristics of natural gas pipelines during the pigging process, *Journal of Natural Gas Science and Engineering* 95 (2021) 104148. <https://doi.org/10.1016/j.jngse.2021.104148>.
- [4] X. Cui, Y. Gao, J. Muggleton, Y. Liu, Superimposed imaging of acoustic wave reflections for the detection of underground nonmetallic pipelines, *Mechanical Systems and Signal Processing* 209 (2024) 111127. <https://doi.org/10.1016/j.ymsp.2024.111127>.
- [5] J. Wang, X. Xiao, L. Peng, J. Wang, Y. He, X. Sheng, Modelling metro-induced environmental vibration by combining physical-numerical and deep learning methods, *Mechanical Systems and Signal Processing* 220 (2024) 111687. <https://doi.org/10.1016/j.ymsp.2024.111687>.
- [6] Y. He, X. Sheng, J. Han, Y. Zhang, X. Xiao, Modeling ground vibration excited by a high-speed train running along a viaduct railway using a new structure-soil interaction method, *Science of The Total Environment* 956 (2024) 177136. <https://doi.org/10.1016/j.scitotenv.2024.177136>.
- [7] F.P. Kopsaftopoulos, S.D. Fassois, Vibration based health monitoring for a lightweight truss structure: Experimental assessment of several statistical time series methods, *Mechanical Systems and Signal Processing* 24 (2010) 1977–1997. <https://doi.org/10.1016/j.ymsp.2010.05.013>.
- [8] C.S. Sakaris, J.S. Sakellariou, S.D. Fassois, A time series generalized functional model based method for vibration-based damage precise localization in structures consisting of 1D, 2D, and 3D elements, *Mechanical Systems and Signal Processing* 74 (2016) 199–213. <https://doi.org/10.1016/j.ymsp.2015.07.014>.
- [9] K.J. Vamvoudakis-Stefanou, J.S. Sakellariou, S.D. Fassois, Vibration-based damage detection for a population of nominally identical structures: Unsupervised Multiple Model (MM) statistical time series type methods, *Mechanical Systems and Signal Processing* 111 (2018) 149–171. <https://doi.org/10.1016/j.ymsp.2018.03.054>.
- [10] N. Tsivouraki, S. Fassois, K. Tserpes, On the random vibration-based progressive fatigue damage detection and classification for thermoplastic coupons under population and operational uncertainty, *Composite Structures* 349–350 (2024) 118524. <https://doi.org/10.1016/j.compstruct.2024.118524>.
- [11] H. Xia, Y.M. Cao, G. De Roeck, Theoretical modeling and characteristic analysis of moving-train induced ground vibrations, *Journal of Sound and Vibration* 329 (2010) 819–832. <https://doi.org/10.1016/j.jsv.2009.10.007>.
- [12] A. Herbut, A study of the reduction of ground vibrations by an active generator, *Soil Dynamics and Earthquake Engineering* 88 (2016) 328–344. <https://doi.org/10.1016/j.soildyn.2016.06.015>.
- [13] Q. He, Y. Yang, J. Yang, S. Zhu, W. Zhai, Experimental investigation of dynamic features and propagation law of ground vibrations induced by a suspended monorail train, *Soil Dynamics and Earthquake Engineering* 183 (2024) 108789. <https://doi.org/10.1016/j.soildyn.2024.108789>.
- [14] Y.B. Yang, L.T. Xie, Y.Z. Liu, J. Li, Analytical solution of ground vibration of a half-space induced by sub- and super-critical harmonic moving loads: Theory and application, *Soil Dynamics and Earthquake Engineering* 187 (2024) 109019. <https://doi.org/10.1016/j.soildyn.2024.109019>.
- [15] M. Wu, B. Wang, Z. Ba, K. Dai, J. Liang, Propagation attenuation of elastic waves in multi-row infinitely

- periodic pile barriers: A closed-form analytical solution, *Engineering Structures* 315 (2024) 118480. <https://doi.org/10.1016/j.engstruct.2024.118480>.
- [16] S. Wang, T. Ma, W. Zhang, Statistical characterization and attenuation of vibration effect for continuous asphalt pavement survey using ground-penetrating radar, *Automation in Construction* 173 (2025) 106057. <https://doi.org/10.1016/j.autcon.2025.106057>.
- [17] Z. Zarei, J. Sadeghi, A. Sarkar, Evaluation of heavy-vehicle-induced vibrations running on asphalt pavements, *Construction and Building Materials* 358 (2022) 129399. <https://doi.org/10.1016/j.conbuildmat.2022.129399>.
- [18] G. Bornitz, *Über die Ausbreitung der von Großkolbenmaschinen erzeugten Bodenschwingungen in die Tiefe*, Springer-Verlag, 2013.
- [19] D.-S. Kim, J.-S. Lee, Propagation and attenuation characteristics of various ground vibrations, *Soil Dynamics and Earthquake Engineering* 19 (2000) 115–126. [https://doi.org/10.1016/S0267-7261\(00\)00002-6](https://doi.org/10.1016/S0267-7261(00)00002-6).
- [20] X. Ren, J. Wu, Y. Tang, J. Yang, Propagation and attenuation characteristics of the vibration in soft soil foundations induced by high-speed trains, *Soil Dynamics and Earthquake Engineering* 117 (2019) 374–383. <https://doi.org/10.1016/j.soildyn.2018.11.004>.
- [21] D. Niu, Y. Deng, H. Mu, J. Chang, Y. Xuan, G. Cao, Attenuation and propagation characteristics of railway load-induced vibration in a loess area, *Transportation Geotechnics* 37 (2022) 100858. <https://doi.org/10.1016/j.trgeo.2022.100858>.
- [22] C. Wang, L. Song, Z. Yuan, J. Fan, State-of-the-art AI-based computational analysis in civil engineering, *Journal of Industrial Information Integration* 33 (2023) 100470. <https://doi.org/10.1016/j.jii.2023.100470>.
- [23] C. Yang, C. Wang, B. Wu, F. Zhao, J. Fan, L. Zhou, Settlement estimation during foundation excavation using pattern analysis and explainable AI modeling, *Automation in Construction* 166 (2024) 105651. <https://doi.org/10.1016/j.autcon.2024.105651>.
- [24] C. Yang, C. Wang, F. Zhao, B. Wu, J. Fan, Y. Zhang, Smart virtual sensing for deep excavations using real-time ensemble graph neural networks, *Automation in Construction* 172 (2025) 106040. <https://doi.org/10.1016/j.autcon.2025.106040>.
- [25] J. Cao, T. Wang, L. Shang, J. Wang, C.-M. Vong, C. Yin, X. Huang, A novel distance estimation algorithm for periodic surface vibrations based on frequency band energy percentage feature, *Mechanical Systems and Signal Processing* 113 (2018) 222–236. <https://doi.org/10.1016/j.ymsp.2017.10.016>.
- [26] M. Monjezi, M. Ghafurikalajahi, A. Bahrami, Prediction of blast-induced ground vibration using artificial neural networks, *Tunnelling and Underground Space Technology* 26 (2011) 46–50. <https://doi.org/10.1016/j.tust.2010.05.002>.
- [27] W. Liu, R. Liang, H. Zhang, Z. Wu, B. Jiang, Deep learning based identification and uncertainty analysis of metro train induced ground-borne vibration, *Mechanical Systems and Signal Processing* 189 (2023) 110062. <https://doi.org/10.1016/j.ymsp.2022.110062>.
- [28] A.K. Verma, T.N. Singh, Intelligent systems for ground vibration measurement: a comparative study, *Engineering with Computers* 27 (2011) 225–233. <https://doi.org/10.1007/s00366-010-0193-7>.
- [29] Y. Jiao, G. Xu, X.-H. Cui, Z. Duan, Y.-Y. Guo, P. He, D.-H. Ji, J.-Y. Li, X.-Y. Li, C. Meng, Y.-M. Peng, S.-K. Tian, J.-Q. Wang, N. Wang, Y.-Y. Wei, H.-S. Xu, F. Yan, C.-H. Yu, Y.-L. Zhao, Q. Qin, The HEPS project, *J Synchrotron Rad* 25 (2018) 1611–1618. <https://doi.org/10.1107/s1600577518012110>.
- [30] IGU SmartSolo, (n.d.). <https://www.smartsolo.com.cn/xl-IGU.html> (accessed May 1, 2025).
- [31] R. Amirikas, A. Bertolini, W. Bialowons, H. Ehrlichmann, D. Elektronen-Synchrotron, *GROUND MOTION & COMPARISON OF VARIOUS SITES*, (2005).
- [32] Suzhou Dongling vibration test instrument Co., Ltd, (n.d.). <https://www.donglingtech.com/> (accessed May 1, 2025).
- [33] B.K. Petersen, M.L. Larma, T.N. Mundhenk, C.P. Santiago, S.K. Kim, J.T. Kim, Deep symbolic regression:

- Recovering mathematical expressions from data via risk-seeking policy gradients, in: 2020. <https://openreview.net/forum?id=m5Qsh0kBQG> (accessed February 26, 2024).
- [34] M. Vastl, J. Kulhánek, J. Kubalík, E. Derner, R. Babuška, SymFormer: End-to-end symbolic regression using transformer-based architecture, (2022). <https://doi.org/10.48550/arXiv.2205.15764>.
- [35] W. Tenachi, R. Ibata, F. Diakogiannis, Deep Symbolic Regression for Physics Guided by Units Constraints: Toward the Automated Discovery of Physical Laws, *The Astrophysical Journal* 959 (2023) 99. <https://doi.org/10.3847/1538-4357/ad014c>.
- [36] S. Hochreiter, J. Schmidhuber, Long Short-term Memory, *Neural Computation* 9 (1997) 1735–80. <https://doi.org/10.1162/neco.1997.9.8.1735>.
- [37] A. Vaswani, N. Shazeer, N. Parmar, J. Uszkoreit, L. Jones, A.N. Gomez, Ł. Kaiser, I. Polosukhin, Attention is all you need, in: *Proceedings of the 31st International Conference on Neural Information Processing Systems*, Curran Associates Inc., Red Hook, NY, USA, 2017: pp. 6000–6010.
- [38] P.-Y. Chen, C. Wang, J.-S. Fan, Multivariate engineering formulas discovery with knowledge-based neural network, *Computer-Aided Civil and Infrastructure Engineering* n/a (n.d.). <https://doi.org/10.1111/mice.13448>.
- [39] S. Yang, Attenuation of Ground Vibration Induced by Dynamical Machinery, in: 1981. <https://www.semanticscholar.org/paper/Attenuation-of-Ground-Vibration-Induced-by-Yang/0d43b1b3b7315076a6a07dd92f0a54446ee0d613> (accessed March 13, 2025).
- [40] X.-J. Yang, Evaluation of Man-Made Ground Vibrations, in: 1995. <https://www.semanticscholar.org/paper/Evaluation-of-Man-Made-Ground-Vibrations-Yang/2d24d0a917c0550e1a252751e22b2c1b484ecf81> (accessed March 13, 2025).
- [41] minimize — SciPy v1.15.2 Manual, (n.d.). <https://docs.scipy.org/doc/scipy/reference/generated/scipy.optimize.minimize.html> (accessed March 13, 2025).